6th European Conference on Computational Mechanics (ECCM 6)
7th European Conference on Computational Fluid Dynamics (ECFD 7)
1115 June 2018, Glasgow, UK

LATTICE BOLTZMANN MODELLING OF PULSATILE FLOW USING MOMENT BOUNDARY CONDITIONS

ZAINAB A. BU SINNAH[1], DAVID I. GRAHAM[1] AND TIM REIS[2]

[1] School of Computing, Electronics and Mathematics, University of Plymouth,
Plymouth PL4 8AA, UK
e-mail: zainab.businnah@plymouth.ac.uk, dgraham@plymouth.ac.uk.

[2] Department of Mathematical Sciences, University of Greenwich,
Greenwich SE10 9LS, UK
e-mail t.reis@greenwich.ac.uk

Key words: Lattice Boltzmann Method, Pulsatile Flow, Moment-Based Boundary Condition.

Abstract. A Lattice Boltzmann Method (LBM) with moment based boundary conditions is used to numerically simulate the two-dimensional flow between parallel plates, driven by a pulsating pressure gradient. The flow is simulated by using a single relaxation time model under both non-slip and Navier-slip boundary conditions. Convergence is investigated by using two distinct approaches. The first approach uses acoustic scaling in which we fix Mach, Reynolds and Womersley numbers whilst varying the LBM relaxation time. Diffusive scaling is used in the second approach - here we fix the Reynolds and Womersley numbers and the relaxation time whilst the Mach number decreases with increasing grid size. For no-slip conditions using acoustic scaling, the numerical method converges, but not always to the appropriate analytical result. However, the diffusive scaling approach performs as expected in this case, showing second-order convergence to the correct analytical result. Convergence to the analytical solution (though not always second-order) is also observed for the simulations with Navier-slip using diffusive scaling.

1 INTRODUCTION

The Lattice Boltzmann Method (LBM) is considered as category of computational fluid dynamics (CFD) methods for fluid simulation. The LBM evolved from the Lattice Gas Automata (LGCA) [13]. The simple model of LBM is the Bhatnagar, Gross and Krook (BGK) collision model [4]. Moreover, the LBE is constructed to recover the Navier-Stokes equations in the macroscopic limit.

Many boundary conditions have been developed for the LBM. The most commonly used are bounce back boundary conditions. In this paper, a moment-based method is used. This imposes constraints on the hydrodynamic moments of the particle distribution function. This method may be viewed as an extension and generalisation of a method

originally proposed by Noble *et. al* [10] for a six-point lattice. Moment-based conditions eliminate the viscosity-dependent error associated with bounce-back and allows the user to impose a variety of hydrodynamic constraints at grid points. This method has already been applied to several flows such as rarefied flow with first order Navier-Maxwell slip boundary conditions [11], and a diffusive slip [3] and no-slip such as [9] and wetting conditions for multiphase flow (Hantsch and Reis) [6], and adiabatic and heat source conditions (Allen and Reis) [1]. In all cases, second order accuracy has been confirmed numerically.

In this paper, we explore the performance of the LBM with moment based boundary conditions to simulate pulsatile flow between parallel plates, subject to both no-slip and Navier-slip conditions at solid boundaries. In Section 2, we introduce the discrete velocity Boltzmann equation and the Lattice Boltzmann Method. We illustrate the moment-based boundary condition in Section 3. In Section 4.1 we give the exact solutions for the pulsatile flow. Section 4.2 shows the results for these simulation and investigates the convergence for (i) fixed Mach, Womersley and Reynolds numbers and varying relaxation time (ii) fixed Womersley and Reynolds numbers and relaxation time and Mach $\sim \delta x \to 0$. Concluding remarks are given in Section 5.

2 THE DISCRETE BOLTZMANN EQUATION

The discrete velocity Boltzmann equation with he BGK collision operator is [12]

$$\partial_t f_\alpha + \mathbf{c}_\alpha . \bigtriangledown f_\alpha = -\frac{1}{\tau}(f_\alpha - f_\alpha^0) + F_\alpha, \tag{1}$$

where $\{\mathbf{c}_\alpha\}$ is a finite set of discrete particle velocities corresponding to the finite set of distribution functions $\{f_\alpha\}$ for the D_2Q_9 lattice (see Figure 1), τ is the relaxation time and F_α is the forcing term.

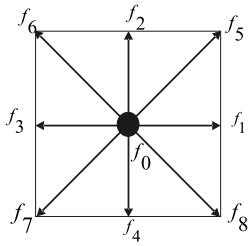

Figure 1: D_2Q_9 Lattice

The BGK collision operator leads to relax the f_α to the equilibrium with the given relaxation time. The functions f_α^0 are the equilibrium distribution functions for the D_2Q_9 model. The first two moments of f_α are density $\rho = \sum_{\alpha=0}^{8} f_\alpha$ and momentum $\rho\mathbf{u} = \sum_{\alpha=0}^{8} \mathbf{c}_\alpha f_\alpha$ the same as the first two moment of f_α^0. The momentum flux tensor is $\mathbf{\Pi} = \sum_{\alpha=0}^{8} \mathbf{c}_\alpha \mathbf{c}_\alpha f_\alpha$ and the equilibrium momentum flux tensor is $\mathbf{\Pi}^0 = PI + \rho\mathbf{uu}$ where I is the Kronecker delta function. The third moment is $\mathbf{Q} = \sum_{i=0}^{8} \mathbf{c}_i \mathbf{c}_i \mathbf{c}_i f_i$.

The evolution equation for the hydrodynamic moments are obtained by taking zero, first and second moments of the discrete velocity Boltzmann equation (1) respectively,

$$\partial_t \rho + \nabla.\rho\mathbf{u} = 0, \quad \partial_t(\rho\mathbf{u}) + \nabla.\mathbf{\Pi} = \mathbf{F}, \quad \partial_t \mathbf{\Pi} + \nabla.\mathbf{Q} \ = -\tfrac{1}{\tau}(\mathbf{\Pi} - \mathbf{\Pi}^0) + \mathbf{Fu} + \mathbf{uF}. \quad (2)$$

The density and momentum with body force $\mathbf{F} = \rho\mathbf{g}$ are conserved by collisions in first and second equation of equations (2). By applying the Chapman Enskog expansion to the discrete velocity Boltzmann equation, we write

$$\mathbf{\Pi} = \mathbf{\Pi}^0 + \tau\mathbf{\Pi}^1 + O(\tau^2), \quad \mathbf{Q} = \mathbf{Q}^0 + \tau\mathbf{Q}^1 + O(\tau^2), \quad \partial_t = \partial_{t_0} + \tau\partial_{t_1} + O(\tau^2), \quad (3)$$

and we find the first order correction to the momentum flux tensor to be $(\mathbf{\Pi}^1)$, which is the Newtonian viscous stress tensor. The stress tensor is $\mathbf{\Pi}^1 = -\frac{1}{3}\rho[(\nabla\mathbf{u}) + (\nabla\mathbf{u})^T] + O(Ma^3)$ where $(\nu = \frac{\tau}{3})$ is the kinematic viscosity and $(\mu = \frac{\tau\rho}{3})$ is the dynamic viscosity. Thus equations (2), include the Continuity and Navier-Stokes equations. The Mach number (M) is defined as $M = \frac{U}{c_s} \ll 1$, where $c_s = \frac{1}{3}$ is the sound speed (in lattice units) and U is taken as a characteristic velocity.

The LBE is found by using the integration on both sides of the equation (1) over a characteristic for time and using the Trapezoidal Rule to integrate and estimate the right hand side. Defining $\overline{f}_\alpha = f_\alpha + \frac{\delta_t}{2\tau}(f_\alpha - f_\alpha^0) - \frac{\delta_t}{2}F_\alpha$, we get

$$\overline{f}_\alpha(x + c_\alpha\delta_t, t + \delta_t) - \overline{f}_\alpha(x,t) = -\frac{1}{\overline{\tau}}\left[\left(\overline{f}_\alpha(x,t) - f_\alpha^0(x,t)\right) - \tau F_\alpha\right], \quad (4)$$

where $\overline{\tau} = \frac{\tau + 0.5\delta_t}{\delta_t}$. Note that the transformation from f_α to $\overline{f}_\alpha$ is required to obtain an explicit algorithm. The associated macroscopic quantities for the transformed variables are

$$\overline{\rho} = \sum_\alpha \overline{f}_\alpha = \rho, \ \overline{\rho\mathbf{u}} = \sum_\alpha \mathbf{c}_\alpha \overline{f}_\alpha = \rho\mathbf{u} + \rho\frac{\delta_t}{2}\mathbf{F}, \quad (5)$$

$$\overline{\Pi} = \sum_\alpha \mathbf{c}_\alpha\mathbf{c}_\alpha\overline{f}_\alpha = \frac{2\tau + \delta_t}{2\tau}\Pi - \frac{\delta_t}{2\tau}\Pi^0 - \frac{\delta_t}{2}(\mathbf{Fu} + \mathbf{uF}). \quad (6)$$

3 MOMENT BOUNDARY CONDITION

At planar boundaries aligned with grid points, the D_2Q_9 LBM post-streaming always has three unknown incoming distributions which can be found from three linearly independent moment conditions. The moment-based boundary methodology involves imposing physical constraints on three linearly independent hydrodynamic moments, from which we obtain the three unknown distribution functions at a boundary.

To apply this condition we consider that we have solid wall at the north and south flow boundaries. After the streaming step, the unknown distribution functions $\overline{f}_4, \overline{f}_7$ and $\overline{f}_8$ at the north boundary and $\overline{f}_2, \overline{f}_5$ and $\overline{f}_6$ at the south boundary.

The Navier-slip boundary condition is implemented by choosing three linearly independent moments from Table (1). Here we choose the tangential momentum ρu_x, vertical velocity momentum ρu_y and the tangential momentum flux tensor Π_{xx} at the wall. We impose them as $\rho u_x = u_s$, $\rho u_y = 0$, $\Pi_{xx} = \frac{\rho}{3} + \rho u_s^2$ where u_s is the slip velocity (we also

note that $p = \frac{\rho}{3}$ is the pressure). The tangential momentum flux tensor is defined as $\Pi_{xx} = \Pi^0_{xx} + \tau\Pi^1_{xx}$. Furthermore, $\Pi^1_{xx} \simeq \partial_x u_x$ and this is zero under either slip or no-slip boundary conditions. At north or south boundaries, then, $\rho\overline{u}_y = 0$, $\rho\overline{u}_x = \rho u_s - \frac{\delta_t}{2}\rho G_x$ and $\overline{\Pi}_{xx} = \frac{\rho}{3} + \rho u_s^2 - \rho G_x u_s$ where $\mathbf{F} = \rho\,(G_x, 0)$ is the body force.

Table 1: Moments at the North and South boundary.

Moments	Combination at the North boundary	Combination at the South boundary
$\rho, \rho u_y, \Pi_{yy}$	$f_4 + f_7 + f_8$	$f_2 + f_5 + f_6$
$\rho u_x, \Pi_{xy}, \Pi_{xyy}$	$f_8 - f_7$	$f_5 - f_6$
$\Pi_{xx}, \Pi_{xxy}, \Pi_{xxyy}$	$f_8 + f_7$	$f_5 + f_6$

Now, we solve the system which is equations (7) to find the unknown distribution functions.

$$\begin{aligned}
\rho\overline{u}_x &= \overline{f}_1 + \overline{f}_5 + \overline{f}_8 - \left(\overline{f}_3 + \overline{f}_6 + \overline{f}_7\right) = \rho u_s - \frac{\delta_t}{2}\rho G_x, \\
\rho\overline{u}_y &= \overline{f}_2 + \overline{f}_5 + \overline{f}_6 - \left(\overline{f}_4 + \overline{f}_7 + \overline{f}_8\right) = 0, \\
\overline{\Pi}_{xx} &= \overline{f}_1 + \overline{f}_5 + \overline{f}_8 + \left(\overline{f}_3 + \overline{f}_6 + \overline{f}_7\right) = \frac{\rho}{3} + \rho u_s^2 - \rho G_x u_s. \qquad (7)
\end{aligned}$$

For example, the unknown distribution functions at the North wall are $\overline{f}_4, \overline{f}_7$ and $\overline{f}_8$

$$\overline{f}_4 = \overline{f}_1 + \overline{f}_2 + \overline{f}_3 + 2\left(\overline{f}_5 + \overline{f}_6\right) - \frac{\rho}{3} - \rho u_s^2 + \rho G_x u_s, \qquad (8)$$

$$\overline{f}_7 = -\overline{f}_3 - \overline{f}_6 + \frac{\rho}{6} + \frac{\delta_t}{4}\rho G_x - \frac{1}{2}\rho u_s + \frac{1}{2}\rho u_s^2 - \frac{\delta_t}{2}\rho G_x u_s, \qquad (9)$$

$$\overline{f}_8 = -\overline{f}_1 - \overline{f}_5 + \frac{\rho}{6} - \frac{\delta_t}{4}\rho G_x + \frac{1}{2}\rho u_s + \frac{1}{2}\rho u_s^2 - \frac{\delta_t}{2}\rho G_x u_s, \qquad (10)$$

where $\rho = \overline{f}_0 + \overline{f}_1 + \overline{f}_3 + 2\left(\overline{f}_2 + \overline{f}_5 + \overline{f}_6\right)$ is found from the definition of the density and $\rho\overline{u}_y$. The slip velocity is proportional to the shear stress at the wall $u_s = l_s\partial_y u_{wall}$ thus, $u_s = -\frac{l_s}{\mu}\Pi_{xy}$ and

$$u_s = \frac{6l_s}{\rho\,(1 + 2\tau + 6l_s)}\left(\overline{f}_1 - \overline{f}_3 + 2\overline{f}_5 - 2\overline{f}_6 + \frac{1}{2}\rho G_x\right) \qquad (11)$$

where l_s is slip length. By using $u_x = u_s = 0$ we can find the unknown distribution functions with non-slip boundary condition.

4 SIMULATIONS

4.1 The exact solutions for pulsatile flow

The 2D pulsatile flow or Womersley flow is driven by a pulsating pressure gradient. The pulsating pressure gradient is implemented by using an equivalent body force $G_x = (2U_c\nu/h^2)\cos(wt)$ in the x-direction where h is the channel half-width, U_c is the centreline speed for the zero frequency case (i.e. Poiseuille flow), $\nu = \frac{U_c h}{Re_{cl}}$ kinematic viscosity and

Re_{cl} is the centreline Reynolds number. The exact solution with a no-slip boundary condition at $u_x = 0$ at $y = \pm h$ is

$$\frac{u_x}{U_c} = \Re\left[\frac{-i}{W_0}\left(1 - \frac{\cosh\left((1+i)W_0\frac{y}{h}\right)}{\cosh\left((1+i)W_0\right)}\right) e^{\frac{i2\pi t}{P}}\right], \tag{12}$$

where $i = \sqrt{-1}$, $W_0 = \sqrt{\frac{w}{2\nu}}h$ is the dimensionless Womersley number, $\omega = \frac{2\pi}{P}$ is the pulsation angular frequency, P is the period and t is the time.

The exact solution with Navier-slip condition $u_x = u_s = l_s|\frac{du_x}{dy}|$ at $y = \pm h$ is

$$\frac{u_x}{U_c} = \Re\left[\left(\frac{u_s}{U_c}\frac{\cosh\left((1+i)\,W_0\frac{y}{h}\right)}{\cosh\left((1+i)\,W_0\right)} + \frac{i}{W_0}\left(1 - \frac{\cosh\left((1+i)\,W_0\frac{y}{h}\right)}{\cosh\left((1+i)\,W_0\right)}\right)\right) e^{\frac{i2\pi t}{P}}\right], \tag{13}$$

$$\frac{u_s}{U_c} = \frac{(i-1)\,K_n \sinh\left((1+i)\,W_0\right)}{W_0\left[\cosh\left((1+i)\,W_0\right) - K_n W_0\,(1+i)\sinh\left((1+i)\,W_0\right)\right]}, \tag{14}$$

where $K_n = \frac{l_s}{h}$ is the dimensionless slip length. Clearly, the exact solutions for no-slip and for Navier slip are both independent of the Reynolds number.

4.2 Simulation

We use the LBM and the boundary conditions discussed above to simulate pulsatile flow. The domain is horizontally periodic. We use computational grids with dimensions $n_x \times n_y$ where $n_x = 2$ and $n_y = 16, 32, 64, 128, 256, 512$. In the lattice units, the channel half width is $h = \frac{n_y}{2}$. The norm error $\overline{L}_2(p)$ over a single period

$$\| \overline{L}\,(p) \|_2 \;=\; \sqrt{\frac{1}{n_\theta}\frac{1}{n_x n_y}\sum_{i,j} |\mathbf{u}_{LBE}\,(l,j,\theta,p) - \mathbf{u}_{Exact}\,(l,j,\theta,p)\,|^2}, \tag{15}$$

where $l = 0, ..., n_x, j = 0, ..., n_y$ and the n_θ is the number of angles in a period (we use $n_\theta = 8$) here. The total computation is run until $t = kP$ where k is the number of periods required for the computations to reach a fully-periodic state.

4.2.1 Simulation under no-slip boundary condition

First simulation: acoustic scaling

In this simulation, the centreline velocity is fixed at $U_c = 0.1$ (in lattice units). This also fixes the Mach number and gives a guarantee that the $M \ll 1$. In this approach, we fix the centreline Reynolds number $Re_{cl} = \frac{U_c h}{\nu}$ as we vary the grid size. This specifies ν and thus gives the relaxation time $\tau = 3\nu$. Fixing the Womersley number means that the period $P = \frac{n_y \pi Re_{cl}}{2W_0^2 U_c}$ thus the timestep $\delta t = 1/P$ is proportional to the grid increment $\delta x = 2/ny$ and thus halves as we double the grid size. The convergence study is carried

out by changing the grid size n_y and the correspondingly changing τ and P to keep the Reynolds and Womersley numbers constant.

We choose Womersley numbers close to those used in the literature such as ([7], [2] and [5]). Figure (2)(a) shows that for low frequency $W_0 = 0.194$ the velocity is parabolic. Similar results are found for a range of Re_{cl} and grid size for this low frequency case. For the high-frequecy case $W_0 = 12.533$, the velocity profile flattens. The simulations successfully predicts this behaviour for different Reynolds numbers ranging from 0.5 to 500. Typical results are shown in Figure (2)(a) and (b) with grid size 64.

For moderate W_0, however, the LBM velocity does not agree with the analytical solution for low Re_{cl}=0.5 as shown in Figures (2)(c) and (d), even as we increase the grid size. Indeed, the simulation appears to converge to a solution different from the exact solution for these parameters. In this case we note that the kinematic viscosity $\nu \approx \frac{n_y}{10}$ increases when the period $P \approx \frac{50n_y}{100}$ increases. Thus, $\lambda = \frac{1}{\tau+0.5}$ is so small that the LBM does not have sufficient time to react to the changing pressure gradient and this remains the case even for large grid sizes. For higher Re_{cl} better agreement is found between numerical and analytical results (see Figure (2)(e)). Here, the rate of relaxation is $\lambda \geq 0.5$ and the period is $P = 50n_y$ so the LBM does have sufficient time to react to the pressure changes in this case.

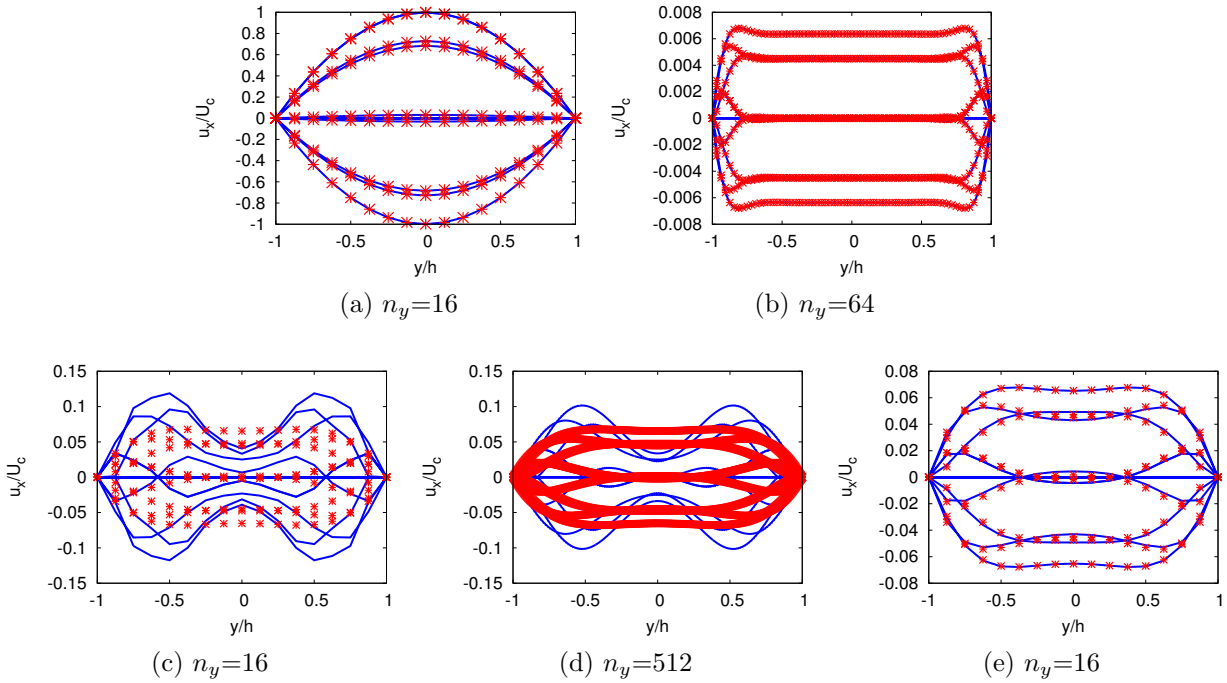

(a) n_y=16 (b) n_y=64

(c) n_y=16 (d) n_y=512 (e) n_y=16

Figure 2: (a) $W_0 = 0.194$, Re_{cl}=5 (b) $W_0 = 12.533$ with Re_{cl}=50 (c), (d) $W_0 = 3.963$, Re_{cl}=0.5 and (e) $W_0 = 3.963$, Re_{cl}=5. Blue lines: LBE; $*$: exact solution.

In this simulation set up, for low Womersley number the norm error flattens off for every Reynolds number (*i.e.* the method does not converge to the analytical solution) as shown in Figure (3)(a). Similar behaviour has been observed by Artoli [2] for $W_0 \approx 15$

and $W_0 \approx 8$ in 2D and 3D. Note also that Latt [8] noted that the error is increased with high grid size in some cases. As the Womersley number increases the method does converge for higher Reynolds number as shown in Figure (3). However, in each case the numerical process does converge as the grid size increases, even if the the results do not necessarily converge to the analytical results. This is demonstrated in Figure (4), where the error between the velocities computed using grid sizes 16 - 256 are compared with those obtained using $n_y = 512$.

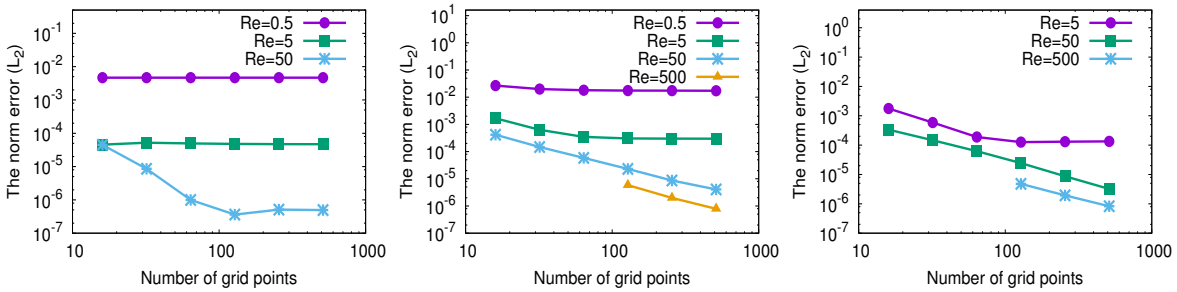

(a) $W_0 = 0.194$ (b) $W_0 = 3.963$ (c) $W_0 = 12.533$

Figure 3: Norm error for acoustic scaling.

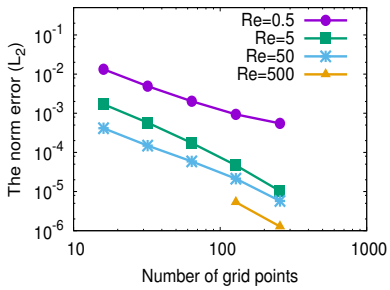

Figure 4: Numerical norm error for acoustic scaling for $W_0 = 3.963$.

Second simulation: diffusive scaling

Noting in some cases the lack of convergence to the analytical solutions of the acoustic scaling approach used above, our second approach uses so-called diffusive scaling. In this case, the relaxation time τ is fixed. Given that this determines ν, we fix the centreline Reynolds number $Re_{cl} = \frac{U_c n_y}{2\nu}$ by varying the centreline velocity U_c proportional to grid spacing $\delta x = 2/n_y$. In this case, fixing the Womersley number leads to a period $P = \frac{3\pi(n_y)^2}{4W_0^2\tau}$ and thus $\delta t \sim \delta x^2$ so the timestep reduces by a factor of 4 as we double the grid size. The convergence study is otherwise similar to that used for the acoustic scaling i.e. we fix Re_{cl} , W_0 and τ as we vary the grid size, and we note that the Mach number is inversely proportional to n_y in this case.

This approach is used by Artoli [2], He and Lou [7], Latt [8] and Cosgrove *et. al* [5]. Initially we choose $\tau = 0.6$ as used by Artoli [2], He and Lou [7].

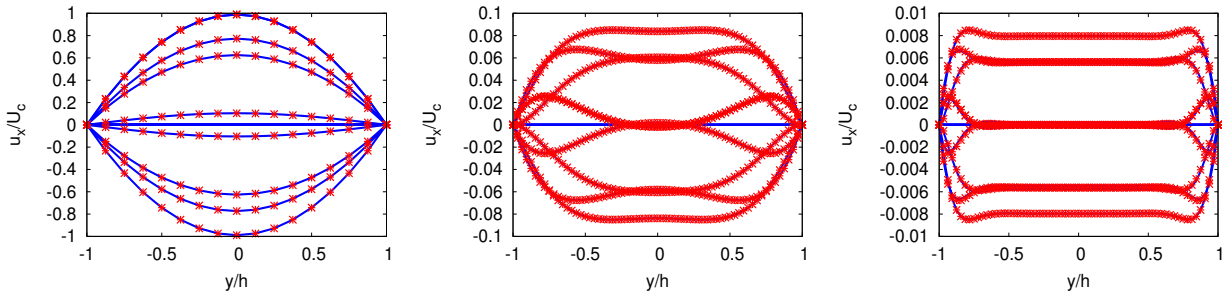

(a) $W_0 = 0.355$ and n_y=16 (b) $W_0 = 3.545$ and n_y=64 (c) $W_0 = 11.201$ and n_y=64

Figure 5: The velocity for τ =0.6. Blue lines: LBE; $*$: exact solution.

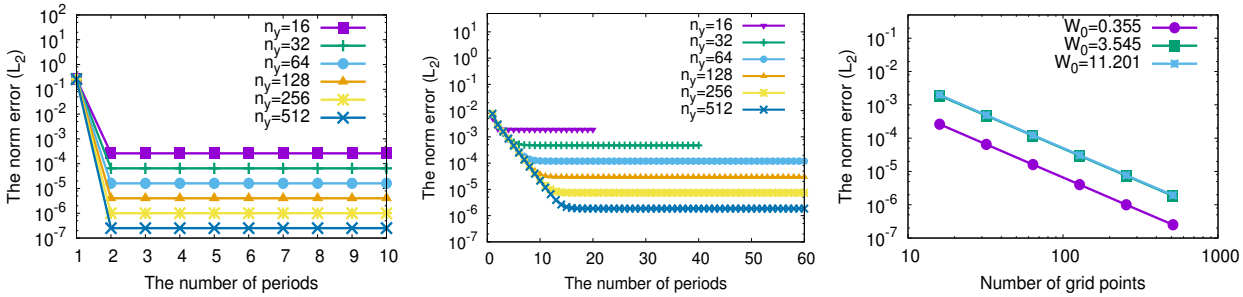

(a) $W_0 = 0.355$ (b) $W_0 = 3.545$ (c)

Figure 6: (a) and (b) are the norm error vs period number, and (c) norm error vs ny for $\tau = 0.6$.

The comparisons between the analytical and numerical solutions of the velocity profile for a range of Womersley numbers are successful as shown in the Figure (5)(a-c). Note that convergence to the final preiodic state is not instantaneous, but must take place over a number of periods. Furthermore, the number of development periods depends upon W_0 and the grid size, as shown in Figure (6)(a), (b).

However, Figure (6) shows second-order convergence is eventually found for a range of W_0. Similar convergence behaviour was found by He and Lou [7], Artoli [2], Latt [8] and Cosgrove *et. al* [5].

4.2.2 The simulation with Navier-slip boundary condition

This simulation is again set up using diffusive scaling i.e. with fixed relaxation time and $\delta t \sim \delta x^2$. In this simulation, we choose a range of different slip lengths to investigate its effect on the velocity profile and the norm error with different Womersley number. Figure (7) demonstrates there is a strong agreement between predictions of the LBE and the exact solution of pulsatile flow. The effect of slip velocity is clear here. For example, Figure (7) shows there are different slip velocities and they are generally larger in magnitude with $K_n = 0.388$ than those for $K_n = 0.194$. Moreover, the slip velocities are reduced with $K_n = 0.0194$ as shown in Figure (7) and the results are very close to those for no-slip.

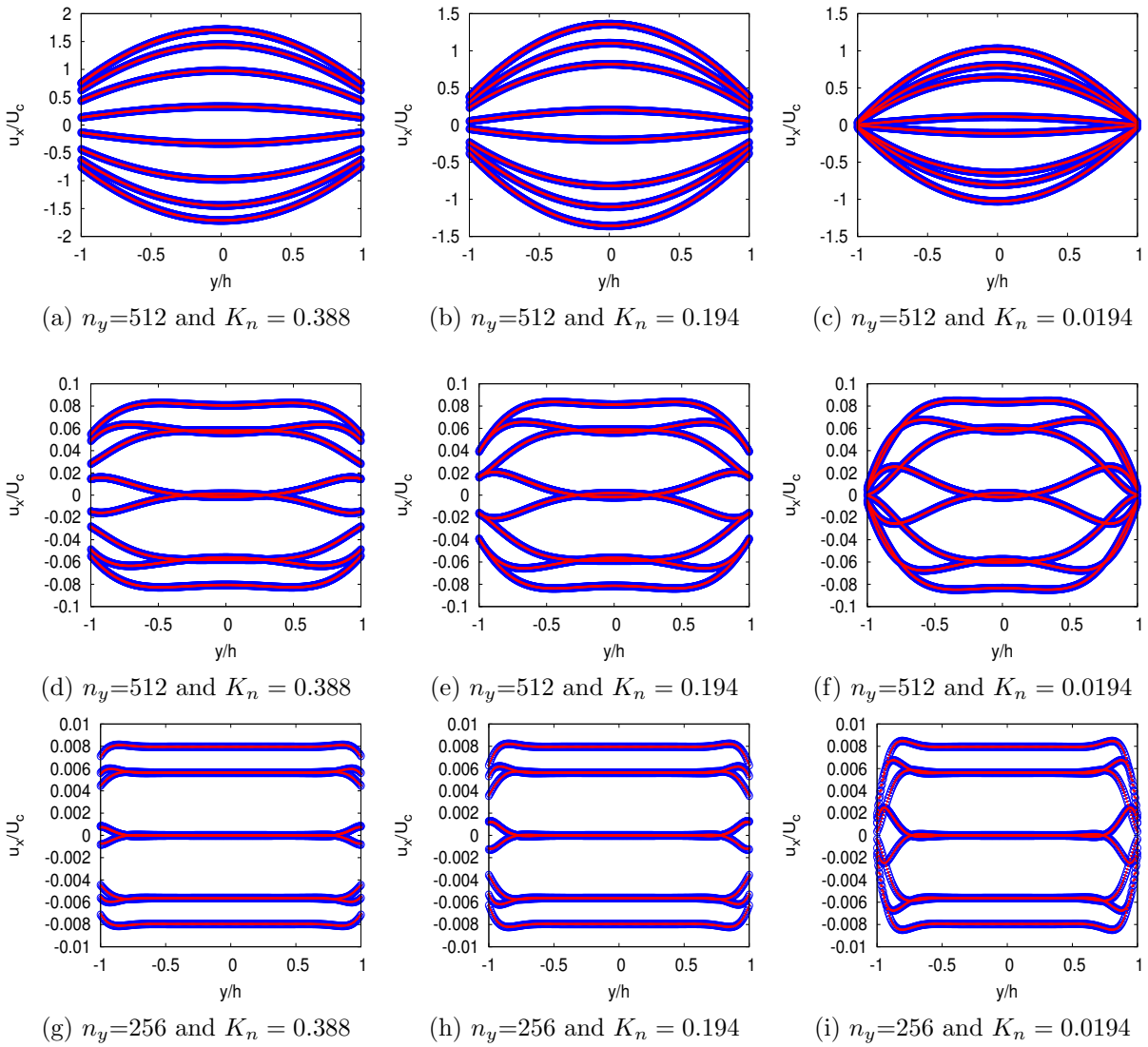

(a) n_y=512 and $K_n = 0.388$ (b) n_y=512 and $K_n = 0.194$ (c) n_y=512 and $K_n = 0.0194$

(d) n_y=512 and $K_n = 0.388$ (e) n_y=512 and $K_n = 0.194$ (f) n_y=512 and $K_n = 0.0194$

(g) n_y=256 and $K_n = 0.388$ (h) n_y=256 and $K_n = 0.194$ (i) n_y=256 and $K_n = 0.0194$

Figure 7: (a), (b) and (c) $W_0 = 0.3545$, $\tau = 0.6$; (d), (e) and (f) $W_0 = 3.545$, τ =0.6; (g),(h) and (i) $W_0 = 11.201$, τ =0.6. Blue: LBE; red: exact solution.

Convergence behaviour for the Navier-slip simulation is shown in Figure (8). We first note that the numerical results and consequent error behaviour are, for given W_0, K_n, completely determined by the τ value. Thus, for given τ, W_0, K_n, we get the same results if we double Re_{cl} as we double the grid size as we get when we fix Re_{cl}. We note that, for $\tau = 6$, convergence is generally second-order independent of W_0 and K_n. For $\tau =$ 0.6 and 0.06, however, convergence becomes approximately first-order for non-zero K_n as the grid size increases, and errors are generally larger for large values of K_n.

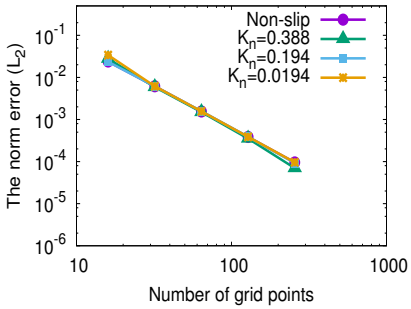

(a) $\tau = 6$ and $W_0 = 0.3545$

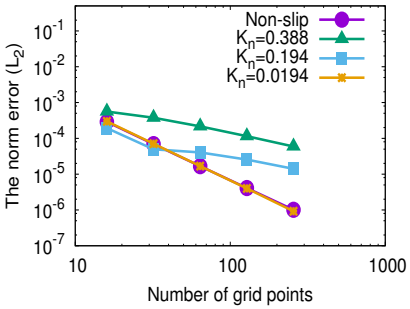

(b) $\tau = 0.6$ and $W_0 = 0.3545$

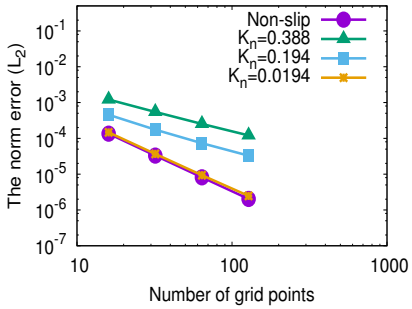

(c) $\tau = 0.06$ and $W_0 = 0.3545$

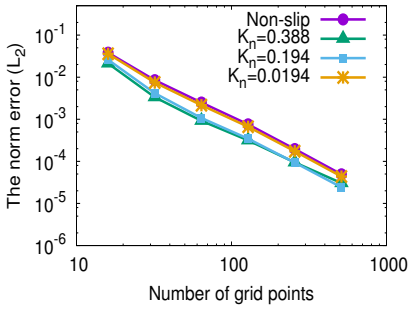

(d) $\tau = 6$ $W_0 = 3.545$

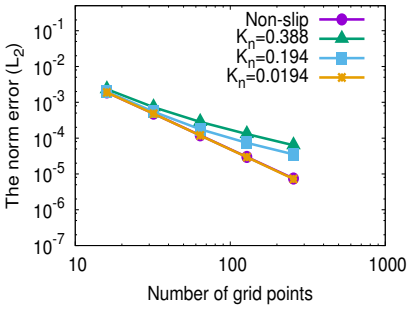

(e) $\tau = 0.6$ and $W_0 = 3.545$

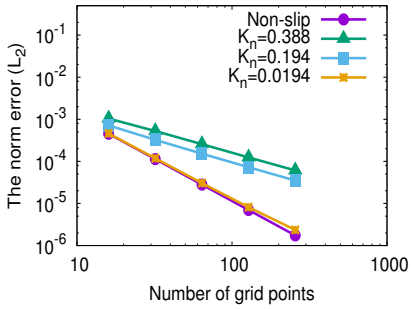

(f) $\tau = 0.06$ and $W_0 = 3.545$

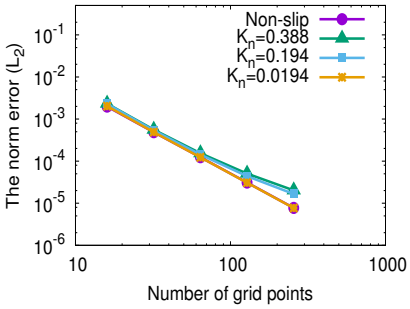

(g) $\tau = 0.6$ and $W_0 = 11.201$

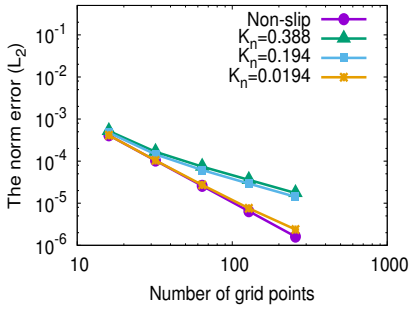

(h) $\tau = 0.06$ and $W_0 = 11.201$

Figure 8: The order of norm error at different K_n with Navier-slip boundary condition.

Since the slip velocity is found as an outcome of the simulations, it is interesting to investigate how the error in slip velocity influences the overall error as shown in Figure (9). Generally, the value of the norm error in the velocity is larger than the value of norm error in the slip velocity at each Womersley number, relaxation time, K_n and grid size which we can see in Figure(8) and Figure(9).

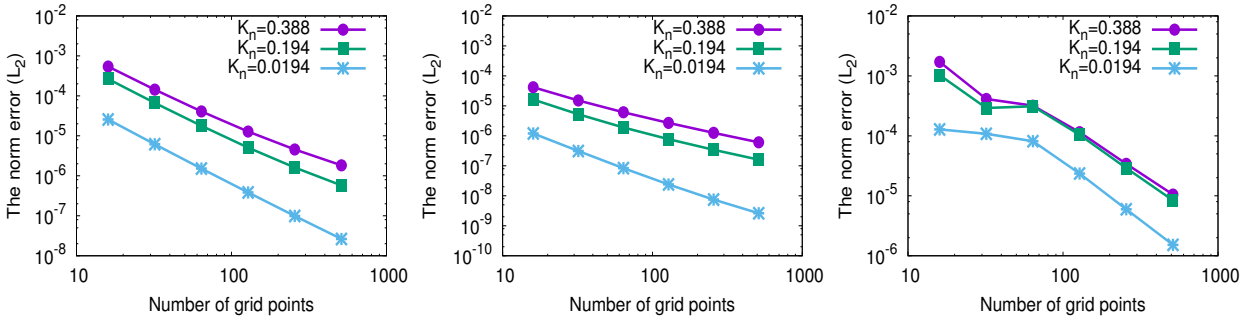

(a) $\tau = 6$ and $W_0 = 0.3545$ (b) $\tau = 0.6$ and $W_0 = 0.3545$ (c) $\tau = 6$ and $W_0 = 3.545$

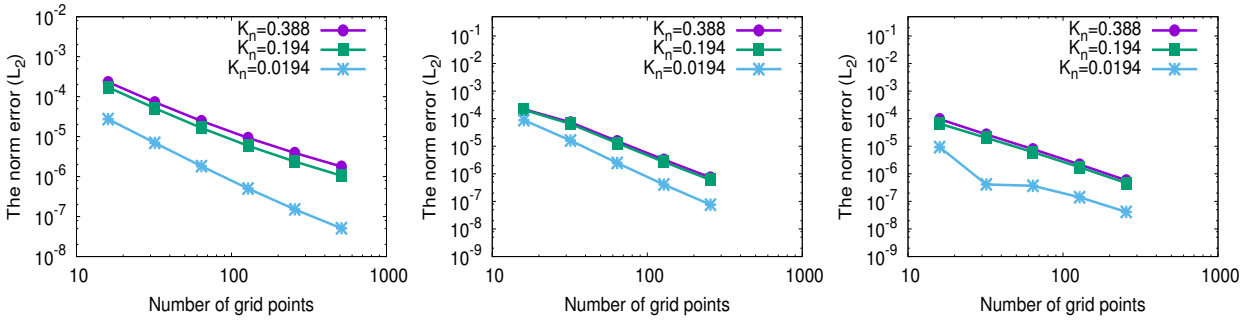

(d) $\tau = 0.6$ and $W_0 = 3.545$ (e) $\tau = 0.6$ and $W_0 = 11.201$ (f) $\tau = 0.06$ and $W_0 = 11.201$

Figure 9: The order of norm error for slip velocity at different K_n with Navier-slip boundary condition.

5 Conclusion

In conclusion, we have performed the numerical simulation of pulsatile flow in two dimensions by using the lattice Boltzmann equation with moment based boundary conditions to impose both no slip and Navier-slip condiitons. Grid convergence studies were performed using two distinct approaches. In the first, acoustic scaling was used in which the Mach, Reynolds and Womersley numbers were all kept constant. In the second approach, diffusive scaling was used. Here, the Reynolds and Womersley numbers, and the lattice relaxation parameter were all kept constant. The velocity profile was computed and compared with analytical solutions. Also, norm errors were computed and the method was shown to be second-order for diffusive scaling for the no-slip case. However, the second order accuracy was not demonstrated for acoustic scaling. The reason for this is that the small relaxation rates required at small Re_{cl}, meaning that the velocity has insufficient time to relax to equilibrium. For Navier-slip, convergence was generally second-order for $\tau = 6$, but appeared to approach first-order for $\tau = 0.6, 0.06$ for non-zero K_n. Errors in computing slip length were generally less than those for the velocity overall.

REFERENCES

[1] R. Allen and T. Reis. Moment-based boundary conditions for lattice Boltzmann simulations of natural convection in cavities. *Prog. Com. Fluid Dyn, an International Journal*, 16(4):216–231, 2016.

[2] AM. Artoli, AG. Hoekstra, and P. Sloot. 3d pulsatile flow with the lattice Boltzmann BGK method. *Int. J. Mod. Phys. C*, 13(08):1119–1134, 2002.

[3] S. Bennett. *A lattice Boltzmann model for diffusion of binary gas mixtures*. PhD thesis, University of Cambridge, 2010.

[4] P. L. Bhatnagar, E. P. Gross, and M. Krook. A model for collision processes in gases. i. small amplitude processes in charged and neutral one-component systems. *Phys. Rev.*, 94(3):511, 1954.

[5] J.A. Cosgrove, J.M. Buick, S.J. Tonge, C.G. Munro, C.A. Greated, and D.M. Campbell. Application of the lattice Boltzmann method to transition in oscillatory channel flow. *J. Phys A: Math. Gen.*, 36(10):2609, 2003.

[6] A. Hantsch, T. Reis, and U. Gross. Moment method boundary conditions for multiphase lattice Boltzmann simulations with partially-wetted walls. *J. Comput Multiphase Flows*, 7(1):1–14, 2015.

[7] X. He and L.-S. Luo. Lattice Boltzmann model for the incompressible Navier–Stokes equation. *J. stat Phys*, 88(3-4):927–944, 1997.

[8] J. Latt. *Hydrodynamic limit of lattice Boltzmann equations*. PhD thesis, University of Geneva, 2007.

[9] S. Mohammed and Tim Reis. Using the lid-driven cavity flow to validate moment-based boundary conditions for the lattice Boltzmann equation. *Arc Mech Eng.*, 64(1):57–74, 2017.

[10] D. R. Noble, S. Chen, J. G. Georgiadis, and R. O. Buckius. A consistent hydrodynamic boundary condition for the lattice Boltzmann method. *Phys. Fluids*, 7(1):203–209, 1995.

[11] T. Reis and P. J. Dellar. Moment-based formulation of Navier–Maxwell slip boundary conditions for lattice Boltzmann simulations of rarefied flows in microchannels. *Phys. Fluids*, 2012.

[12] X. Shan, X.-F. Yuan, and H. Chen. Kinetic theory representation of hydrodynamics: a way beyond the Navier-Stokes equation. *J. Fluid Mech.*, 550(1):413–441, 2006.

[13] D.A. Wolf-Gladrow. *Lattice-Gas Cellular Automata and Lattice Boltzmann models: An Introduction*. Springer Science & Business Media, 2000.